Time-Resolved *In Situ* Imaging of Strain Localization in Draupne Shale under Triaxial Compression

Aldritt Scaria Madathiparambil[1], Kim Robert Tekseth,[1] Fredrik K. Mürer,[1,2] Benoît Cordonnier,[3,4]
Nicolaine Agofack,[5] Jessica McBeck,[3] Pierre Cerasi,[5] François Renard[3,6] Basab Chattopadhyay,[1]
and Dag W. Breiby[1,7,*]

[1]*Department of Physics, Norwegian University of Science and Technology (NTNU), Høgskoleringen 5,
7491 Trondheim, Norway*
[2]*SINTEF Helgeland AS, Halvor Heyerdahls vei 33, 8626 Mo i Rana, Norway*
[3]*The Njord Centre, Departments of Geosciences and Physics, University of Oslo, Oslo, Norway*
[4]*ESRF – The European Synchrotron, CS40220, Grenoble 38043, France*
[5]*SINTEF Industry, Applied Geoscience Department, 7465 Trondheim, Norway*
[6]*ISTerre, University Grenoble Alpes, Grenoble INP, CNRS, IRD, University Gustave Eiffel, Grenoble, France*
[7]*Department of Microsystems, University of South-Eastern Norway (USN), 3184 Borre, Norway*

Understanding the mechanical behavior of rocks is crucial in subsurface activities, including storage of carbon dioxide and hydrogen gases, which both rely on shale caprocks as potential sealing barriers. Several current large-scale initiatives focus on potential carbon storage in North Sea aquifers. The Draupne Formation contains a series of shale layers interbedded with sandstone layers, the overall thickness of which varies in the range from tens to hundreds of meters. Injection of carbon dioxide into the underlying sandstone reservoirs leads to changes in the surrounding stress field, which can result in fault reactivation or the creation of microfractures, and thus, alter the performance of the shale caprock. Time-resolved microcomputed tomography (4D μCT) has, in recent years, become a powerful technique for studying the mechanical properties of rocks under stress conditions similar to those prevailing in geological reservoirs. Here, we present results from experiments performed on Draupne shale using a triaxial rig combined with 4D μCT based on synchrotron radiation. Detailed mechanical analysis of the tomography datasets by digital volume correlation reveals the three-dimensional pattern of the temporally evolving deformation field. Intermittent bursts of deformation at different locations within the specimen are observed, which eventually evolve into a major fracture plane extending laterally across the whole sample. This study suggests that the pseudolinear-elastic-appearing behavior in the macroscopic stress-strain relationship previously reported for Draupne shale samples could consist of a series of irreversible processes occurring at various weak points within the sample. The combination of 4D μCT imaging with strain analysis enables *in situ* investigations of deformation processes via quantification of shear and volumetric strains within the sample, thus providing an improved understanding of the fracture dynamics of shales.

I. INTRODUCTION

The geomechanical response of organic-rich shales to external stress is important knowledge because these materials play a crucial role in a range of environmentally and industrially important processes, including the petroleum industry, CO_2 storage, and H_2 storage. Shale caprocks are exposed to significant loading due to both natural geological stresses, such as thermal stresses and high fluid pressure, and industrial stresses like drilling, fracturing, and fluid injection. The microscale mechanical response of stressed shale greatly affects the stability of the formations, also at much longer length scales of kilometers. Shale rocks may contain multiple fractures that coalesce under stress, causing a transition from stable-to-unstable fracture growth [1,2]. Understanding these processes of fracture formation, eventually leading to macroscopic failure, is critical for a wide range of applications. The influence of fracture development within shales on the permeability of fluids during CO_2 injection and storage remains poorly understood. This lack of knowledge can largely be ascribed to the microscale complexity and heterogeneity of shales [2–5]. Recent studies have focused on the potential for the storage of CO_2 in saline aquifers, coal seams, and

*dag.breiby@ntnu.no

depleted oil and gas reservoirs [6–8]. Geological formations containing porous sandstone reservoirs capped with low-porosity low-permeability caprocks are excellent candidates for CO_2 storage [6]. Shale formations that are around a hundred meters thick act as the caprock for most of these reservoirs. Studies have shown that shale-capped formations tend to adsorb CO_2 and have the potential to inject and store CO_2 [9]. Current academic studies and several full-scale industrial efforts are focusing on evaluating the potential for the storage of CO_2 in the seabed of the North Sea and elsewhere [10,11].

Triaxial mechanical testing, sometimes applied to full-size (12 inch) cores, remains the workhorse for characterizing the mechanical properties of rocks. However, to refine the theoretical models of mechanical behavior for rock systems with highly differing properties, microscopic insights that cannot be gained from macroscopic testing alone are increasingly desired [12]. Imaging techniques like scanning electron microscopy (SEM), sometimes combined with focused-ion-beam milling, can be used to acquire high-resolution images and chemical information through spectroscopy [13]. X-ray diffraction (XRD) is also extensively used for mineral identification. During the last decade, x-ray microcomputed tomography (μCT) has been increasingly used for the nondestructive visualization and mineral quantification of geological samples in three dimensions [14,15]. Using μCT, it is possible to investigate the pore-network properties, microtextures, fractures, and transport properties at spatial resolutions down to, and below, the micrometer level [16]. Recently, time-resolved x-ray microtomography (4D μCT) has opened the possibility of monitoring dynamic processes like mechanical responses and fluid penetration of geomaterials [17,18]. The advent of triaxial test cells compatible with μCT has facilitated investigating the stress- and time-dependent deformation of rock samples [19–22]. We note that neutron-computed tomography is also increasingly used to this end [23,24]. Additional μCT techniques have -recently been introduced to the rock-physics community, e.g., those with diffraction contrast [25] and based on coherent imaging [26,27].

In situ three-dimensional (3D) time-resolved x-ray imaging in combination with digital volume-correlation (DVC) analysis [28,29] is demonstrated to provide detailed information about the evolution of microscopic and macroscopic strain fields at micrometer-scale spatial resolution [17,18,23]. DVC algorithms find the displacement field that best maps each small subvolume (e.g., $10 \times 10 \times 10$ voxels) within a 3D μCT dataset recorded at one time step onto another μCT dataset recorded at a later time step [29]. This is achieved by identifying similar density patterns within those subvolumes and finding the local minute translations, rotations, and dilations that maximize the correlation between pairs of sequential tomograms. DVC is able to capture small systematic movements within the sample that are practically impossible to detect by just observing the tomographic images. Maps showing the 3D displacement and/or strain fields give insights into the mechanical properties of rock samples [30]. Quantitative studies of grain adjustments and rotations at the microscale and the shear-strain distribution in rock samples have been reported. The combination of μCT monitoring and mechanical testing can assist in predicting reservoir properties of the rocks by analyzing the response of porosity and permeability to mechanical stress [30,31].

Stress and strain localization proceeds by destructive microevents that tend to concentrate in weak areas of the specimen [30]. In clay-rich rocks like shales, the dominant micromechanisms leading to strain localization inside shear bands are known to be rotation and decohesion at the grain scale [30]. Also, in rocks, the development of well-defined cracks occurs due to local micromechanical events and the coalescence of microcracks. Strain localization is commonly observed in clayey specimens and can form either a single failure plane or multiple parallel failure planes, depending on the uniformity of the specimen's initial density, the tendency to dilate or to contract, and the boundary conditions [32]. Dilation and compaction are directly linked to the overconsolidation ratio of the clay specimen, that is, the highest overburden (here, axial) stress previously exposed to the sample divided by the current overburden stress.

The present study aims to investigate the mechanical properties of Draupne shale from the North Sea, a caprock recently receiving extensive attention because of its potential for permanent storage of the greenhouse gas CO_2 in the underlying porous sandstone [5,32]. Time-resolved synchrotron μCT combined with DVC analysis is used to estimate the 3D strain distribution throughout a centimeter-sized core of Draupne shale under jacketed triaxial loading. We apply increasing axial compressive stress, oriented perpendicular to the lamination bedding planes, combined with constant confining (lateral) stress to replicate the conditions at a depth of about 2.6 km in the seabed where the samples were obtained. Using DVC analysis, the 3D local strain-displacement field is obtained from the *in situ* CT data. Based mainly on the calculated volumetric strain and the von Mises equivalent strain, we discuss, in detail, the dynamics of strain localization in the Draupne shale as the sample undergoes brittle failure.

II. MATERIALS AND METHODS

A. Shale sample

The sample used in this study was collected at a depth of 2575 m from a borehole in the Draupne Formation. Draupne shale is a caprock that is a low-permeable, homogeneous, and anisotropic black shale with a porosity of about 12% [5,33]. The total organic content of the sample core is reported to be 6–8%, and the permeability is

estimated to be less than 3.2×10^{-22} m^2 (3.2 nDarcy) with a critical pore throat size of 9 nm [4,5]. The very same sample core has been characterized using SEM, XRD, mechanical tests, and permeability measurements [2,3,34]. XRD studies have indicated the presence of more than 60% clay [4]. To prevent damage and drying in contact with air, the core was kept submerged in Marcol™ oil during all stages of sample preparation. An electric drill was used to prepare the 5-mm-diameter cylindrical sample, with its bedding planes perpendicular to the symmetry axis of the cylinder. The cylinder end surfaces were polished to obtain a specimen with a length of 10 mm and right angles for stable mechanical contact.

B. HADES triaxial rig

The shale core sample was deformed *in situ* under triaxial-loading conditions using the HADES rig, cf. Figure 1, installed at beamline ID19 at the European Synchrotron Radiation Facility (ESRF) [20]. This apparatus has a low x-ray attenuation for photon energies >60 keV and can apply stresses both axially (up to 200 MPa) and radially (up to 100 MPa) at temperatures up to 200 °C, while the external fluid ("pore") pressure can be varied from 0.1 to 100 MPa. The body of the rig is constructed from a single piece of titanium with a wall thickness of about 5 mm at the sample location. The sample was saturated with brine (3.6-wt % NaCl) at the same NaCl concentration as that of the native pore fluid prior to loading. The pore fluid pressure in the HADES apparatus was controlled by two hydraulic pumps, one for the pore fluid inlet and the other for the outlet, which could be used in either constant-pressure or constant-flow-rate modes with predefined ramps. The sample was installed between two stainless-steel pistons, with the axial loading imposed by the movable upper piston. Two independent pumps controlled the confining pressure and the axial load. A Viton™ fluoropolymer elastomer encased the rock sample, and the confining pressure was applied on this jacket using silicone oil.

The chosen coordinate system was with the z axis parallel to the cylinder axis, coinciding with the direction of the axial stress, σ_{ax}, and with the x-y plane perpendicular to σ_{ax}. The differential stress, σ_{zz}, was calculated as

$$\sigma_{zz} = \sigma_{ax} - (\sigma_{conf} + \sigma_{pore}) - \sigma_{friction}. \tag{1}$$

Here, σ_{ax}, σ_{conf}, and σ_{pore} denote the applied axial stress, confining pressure, and pore pressure, respectively. The frictional stress, $\sigma_{friction}$, is caused by the mechanics of the HADES setup and is determined from a range of previous experiments to equal approximately (18.1 ± 0.1) MPa. A linear variable differential transformer (LVDT) incorporated into the HADES rig was used to measure axial shortening, and thus, the axial strain, ε_{zz}, of the sample.

The time-resolved axial strain, ε_{zz}, was also obtained from the 3D x-ray images by measuring the shortening of the rock core between the two pistons.

C. Time-lapse microcomputed tomography acquisition

Measurements were performed using the "white" x-ray beam option at ESRF ID19, with a rectangular cross section (5×10 mm^2, defined by slits upstream of the experimental hutch) to image the entire sample inside the HADES rig. A PCO EDGE 5.5 RS detector was used to acquire the projections. Due to x-ray adsorption by the walls of the rig, the equivalent x-ray energy crossing the sample was close to 70 keV. To monitor sample deformation, the stress was increased stepwise and x-ray CT data were acquired while the stress was kept constant. This quasistatic approach was used to reduce the problem of sample movements during the scan, potentially blurring the 3D images. After each stress-step increment, the apparatus was rotated by 180° about a vertical axis, while acquiring 2500 radiographic x-ray projections with a total scan time of about 65 s, giving an effective reconstructed voxel size of (6.5 μm)^3. Every 2 min, a new tomographic scan was started to obtain effectively 4D (i.e., time-resolved 3D) images as the sample was mechanically stressed and deformed. In total, 90 full tomograms were recorded, and the full experiment including stress and pressure ramps lasted nearly 16 h. The experiment was performed at ambient temperature (24 °C). The tomograms were reconstructed using the software PyHST2 [35], involving filtered back-projection coupled with Paganin's propagation-based phase-contrast algorithm [34]. The grayscale value of each voxel in the tomogram was proportional to the x-ray attenuation coefficient, which was a function of density and atomic number. Bright gray levels in the tomogram corresponded to highly attenuating high-density regions, dark gray values were lightly attenuating minerals, and intermediate gray levels corresponded to voxels containing intermediate and/or a subresolution mixture of high- and low-attenuation minerals.

The experimental loading path is displayed in Fig. 1(a); see also Table S1 within the Supplemental Material [36]. The experiment was stress controlled and designed to track damage accumulation and shear localization towards macroscopic failure. The experiment may naturally be divided into the following three parts, as visualized in Fig. 1: stage O, with the initial loading; stage A, in which σ_{zz} was increased up to fracturing; and stage B, in which σ_{zz} was kept constant. An unload-load and a load-unload loop were incorporated in stage O [Fig. 1(a)] to assess the elastic properties of the sample; the first loop should, in principle, provide the bulk modulus and the second loop the Young's modulus; however, these measurements could not be reliably interpreted because, at this early stage of the experiment, the sample was not yet fully settled
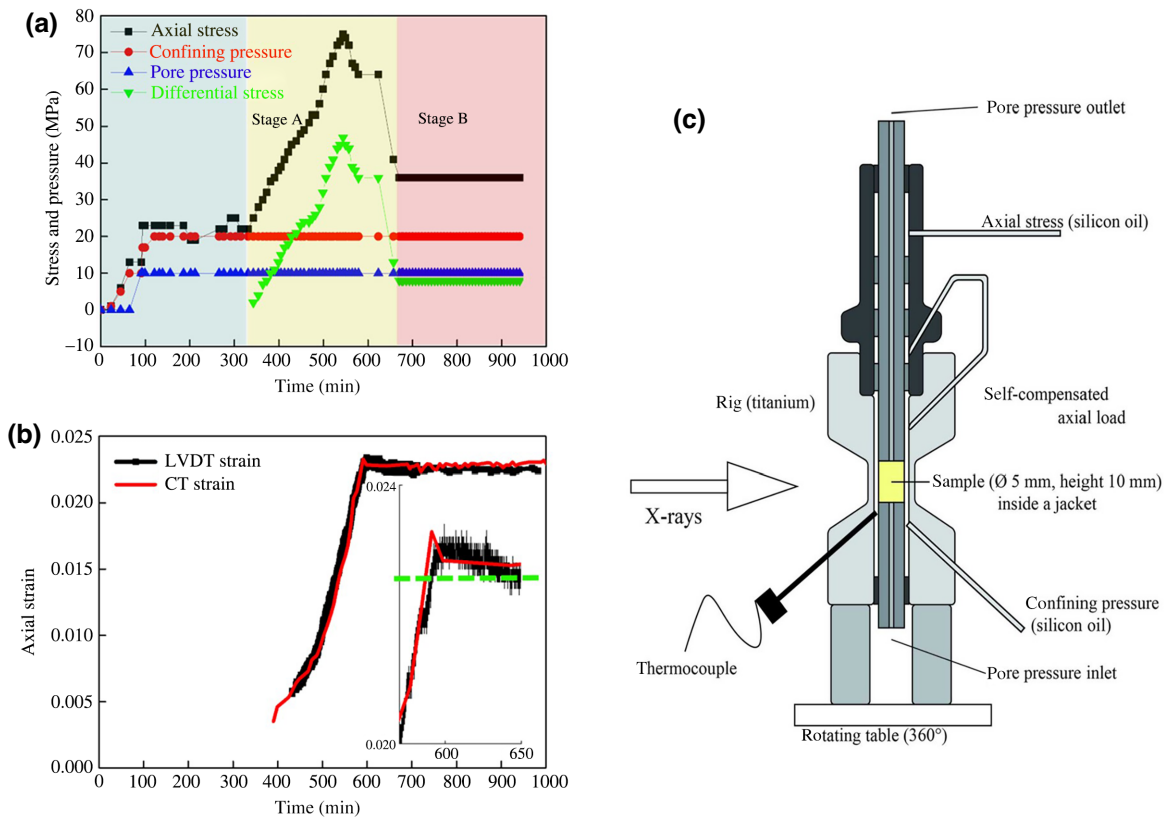
FIG. 1.   Overview of the experiment. (a) Axial stress, σ_{ax}; confining pressure, σ_{conf}; pore pressure, σ_{pore}; and differential stress, σ_{zz}, are plotted as function of time during the experiment. Stage O (consolidation) is shaded in light gray, stage A (axial stress increase) is shaded in yellow, and stage B (constant stress) in light red. Peak axial stress precedes the brittle failure of the core sample. (b) Axial strain, ε_{zz}, as function of time obtained from CT data (red) and from the LVDT measurement (black). Data points for times <400 min are not reliable, owing to minor sample shifts. Inset highlights strain evolution around the fracture event, revealing that the sample expands just after fracturing. Here, axial compression strain is plotted as being positive. Green dashed line indicates the long-term asymptote of axial strain. (c) Sketch of the HADES cell (reproduced from Ref. [20] with permission from IUCr).

in the rig and shifted a little between subsequent stress increments.

During stage O, the pore pressure, confining pressure, and axial stress were increased up to 10, 20, and 22 MPa, respectively. After reaching these values, the confining and pore pressures were kept constant, while the differential stress was stepwise further increased to a maximum of $\sigma_{zz} \sim 48$ MPa (for σ_{ax} of about 75 MPa) and the sample deformed with an average axial strain rate of $(2.1 \pm 0.1) \times 10^{-6}$ s^{-1} [Fig. 1(b)]. This strain rate was chosen to fit the desired stress path with expected peak stress into the time allotted at the synchrotron. Upon reaching peak stress, the material was no longer able to support the applied stress and underwent brittle failure. The axial stress was subsequently reduced to 36 MPa; this was a differential stress level that the shale could sustain without further large deformations for the remainder of the experiment. Because of the rather high axial loading rate, combined with the extremely low permeability of the Draupne shale, it should be noted that, even though the

externally controlled confining pressure and liquid pressure were kept constant, the actual pore pressure inside the rock sample was likely to have increased during the experiment. Experimental data suggesting a Skempton A value of around 0.3 [37] are provided in the Supplemental Material (Text S4) [36]. These considerations imply that, at failure, the effective confining pressure was probably lower than the values provided by the pore-pressure transducers.

D. Digital volume-correlation analysis

DVC was performed using the open-source software Tomowarp2 [29], which, through interpolation methods, returned the incremental 3D displacement field, $\mathbf{u}(\mathbf{r},t)$, between subsequent pairs of tomograms. For most of the DVC calculations, the chosen region of interest was fully contained within the rock sample to suppress disturbing features from the jacket (rubber sleeve) and irregularities on the surface of the sample. An example of DVC

analysis performed for the full field of view is provided in the Supplemental Material [36]; the displacement fields of both the shale sample and the polymer sleeve are visualized in Fig. S4.

The DVC spatial resolution is necessarily inferior to the CT's raw-data resolution, depending on the chosen node spacing. Technically, both the node spacing and the correlation window size are known to strongly influence the magnitude of the strain estimated by the DVC algorithm [28]. The local correlation between the two datasets is quantified with a *correlation coefficient* ranging from 0 (no correlation) to 1 (full correlation) [29]. We used a node spacing of 20 voxels (130 μm) with a cubic correlation window of 10 voxels in size length [volume of (65 μm)^3]. These parameters were kept fixed for all the calculations and were selected following tests to investigate their influence on the resolution; see the Supplemental Material (Text S3) [36]. An outcome of these tests is that we consider, consistent with previous reports [31,38], the obtained displacement and strain fields to be quantitatively reliable only for comparisons between different regions and times within the sample, while the absolute strain values are much more uncertain.

From the series of 3D displacement fields, the incremental second-rank three-dimensional strain-tensor field, $\varepsilon(\mathbf{r},t)$, was calculated, revealing the changes that occurred within the time interval between the acquisitions of the pair of tomograms used in the calculation. The tomograms used for the DVC calculations were chosen at regular intervals of the macroscopic axial strain, specifically about 0.002, which corresponded to an LVDT increment of about 20 μm. We denoted a DVC time point as, for example, ix(44,45), which signified that the ninth pair of tomograms used in the DVC calculation were acquired with the first at a differential stress of 44 MPa and the second at 45 MPa. The enumerated pairs of tomograms used for the DVC analysis can be read from Fig. 2 and Table S1 within the Supplemental Material [36].

III. RESULTS

A. Macroscopic stress and strain

The macroscopic stress-strain behavior in stage A of the shale sample is shown in Fig. 2. As indicated by the straight line, we observed essentially linear behavior during loading up to $\sigma_{zz} = (39 \pm 2)$ MPa, followed by an increasing ductility when approaching the peak stress. After the peak stress was reached, the stress dropped rapidly, and the curve became nearly horizontal. Because shales are highly anisotropic, their mechanical properties will vary with the orientation of the shale bedding planes relative to the core axis [39,40]. Prior to the linear regime of the stress-strain plot, i.e., in stage O, we observed an initial nonlinear response (not shown in Fig. 2), which
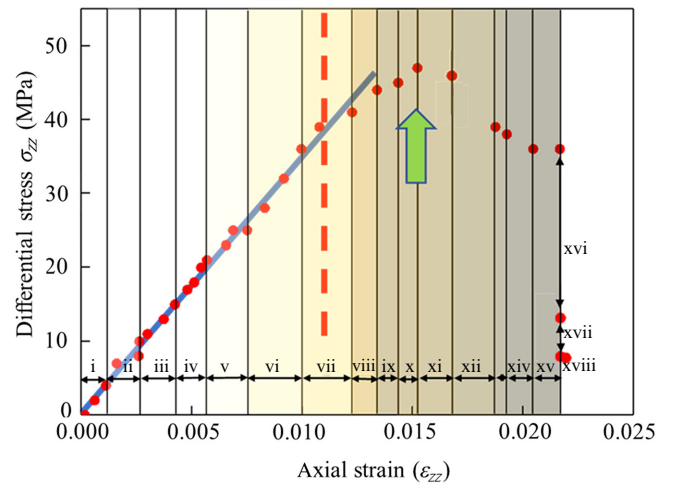

FIG. 2. Differential compressive stress, σ_{zz}, plotted as a function of axial strain, ε_{zz}, during the experiment. Superposed straight gray line suggests an almost linear stress-strain relationship for axial strain levels <0.01. Vertical dashed red line gives the approximate yielding point, and green arrow indicates the peak stress at failure. Roman numerals give the DVC time-step intervals, with i–xv corresponding to stage A in Fig. 1.

could be ascribed to fine adjustments or shifts of the specimen in the rig and the closing of preexisting cracks and pores in the sample under increasing stress. The ostensible interpretation of the stress-strain data in Fig. 2 is that the shale rock exhibits linear elastic behavior. The maximum axial strain, ε_{zz}, consistent with such pseudoelastic behavior, as judged from the macroscopic stress-strain curve in Fig. 2, would be about 0.011 ± 0.001. Estimating the mechanical properties of the sample from the pseudolinear portion of the stress-strain curve, using a linear fit, suggests a Young's modulus of $E = (3.6 \pm 0.2)$ GPa. While this estimate correlates well with reported values obtained for uniaxial compression tests on Draupne shales [40], we demonstrate in the following analysis that this apparently elastic behavior arises despite a series of small, perhaps irreversible, deformation events.

The yield point, defined as where the stress-strain curve starts to deviate from the linear fit, was at a stress level of about 70% of the maximum σ_{zz} (Fig. 2). Beyond this point, the common interpretation [15,17,30,41,42] is that permanent and irreversible deformation and cracks develop in the sample, initially located at soft spots or other defects. These intermittent deformations are generally thought to localize and to grow stably as additional stress is added to reach the overall failure of the sample. Note that, with the resolution of this μCT experiment, these microscopic deformations cannot be seen directly, as they are smaller than the voxel size. The approximate onset of the unstable crack growth in the sample is indicated by the green arrow in Fig. 2, occurring within $97\% \pm 2\%$ of the maximum differential stress.

B. Direct μ-CT observations

Selected views of the sample, before and after the development of the macroscopic primary fracture across the sample, are provided in Fig. 3. This large macroscopic fracture extending laterally throughout the whole sample developed near the upper piston and was aligned predominantly along a plane with an inclination angle of $38° \pm 3°$ with respect to the direction of maximum compressive stress, σ_{zz} (i.e., the cylinder axis z). Cross sections of the reconstructed tomograms reveal the presence of natural fractures in the shale sample at low axial stress [Figs. 3(a1) and 3(b1)]. The majority of microcracks and pores in Draupne shales are at the submicron scale [5], and consequently, below the spatial resolution of these images. Natural fractures were found at several locations in the sample. The same location in different scans was chosen for comparison [Figs. 3(a1)–3(d1)], carefully correcting for the length of the sample gradually being shortened during the experiment. With increasing σ_{zz}, natural fractures initially present at different positions in the sample were observed to close, in agreement with reported observations of stress-induced closing of preexisting cracks and pores in shales and other sedimentary rock systems [40].

Preceding stage B, the sample fractured, and the two portions of rock were observed to behave as two rigid bodies sliding on top of each other [Figs. 3(c2)–3(d2)]. The differential stress was then maintained at 8 MPa until the end of the experiment. Close inspection of Fig. 1(b) also reveals that the specimen, in fact, expands in the axial direction (ε_{zz} decreases) slightly during the first minutes after failure, which is a hallmark of (semi)brittle failure [43]. The sample expansion was also observed in the DVC analysis (data not shown). During the later parts of stage B, the (small) strain events present are located mainly along the fracture plane and at the top and bottom regions of the sample.

C. Microscopic displacement field

To study the microscopic deformation processes towards sample failure, the incremental displacement vector field, $\mathbf{u}(\mathbf{r}, t)$, was obtained by DVC, and is visualized in Fig. 4. The 3D displacement field, $\mathbf{u}(\mathbf{r}, t)$, gives a microscopic view of deformations within the sample. Upon comparing the time steps from v(21,25) up to x(45,47), the initially homogenous deformation field develops via a rotation-rich state into a highly complex state, signifying sample fracture. It is clear from Fig. 4(a) that nonhomogenous deformations are present at least from ix(44,45), and a sliding block is seen for xvii(13,8) onwards, similar to that reported for other rocks like sandstone [43]. Note the clear shear zone seen across the fracture in Fig. 4(b), with displacements in opposite directions. The local deformation field is homogeneous within the blocks, revealing their rigid nature. The displacement field, $\mathbf{u}(\mathbf{r}, t)$, both in 3D and
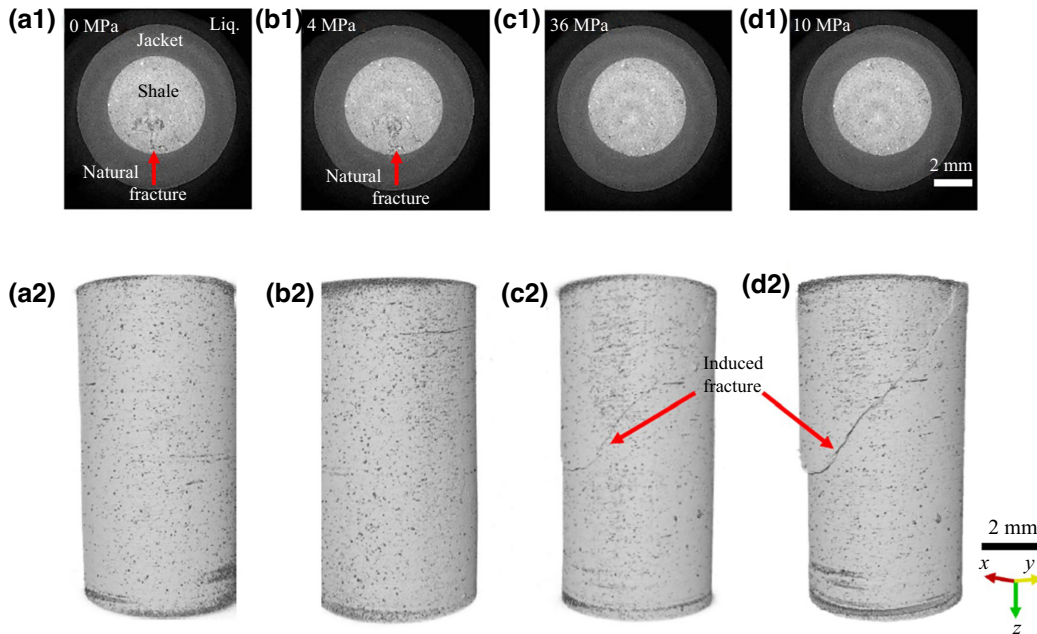

FIG. 3. Selected μCT tomograms of the shale sample (a),(b) before (stage A) and (c),(d) after (stage B) sample failure with the formation of an induced primary fracture spanning across the sample. Top row shows cross sections perpendicular to the core-sample axis; all are obtained at the same axial location at 1.6 mm from the bottom of the sample, showing the closing of preexisting natural fractures upon increasing differential stress, σ_{zz}. Natural fractures seen in the sample (here), as indicated by the red arrows in (a1),(b1) have closed at the higher stress states in (c),(d). Bottom row gives 3D perspective views of the specimen at the same states as in (a1)−(d1), clearly revealing the induced macroscopic primary fracture after failure.

for central 2D axial cross sections, for all the time steps, are shown in Figs. S5 and S6 within the Supplemental Material [36].

Immediately before failure, a pronounced rotational strain state was observed, cf. xiii(39,38). Rotational strain about an axis perpendicular to the applied stress is a known mechanism associated with linear elastic fracture mechanics [30,44], but we are not aware of earlier reported similarly clear microscopic 3D data showing this effect in rocks. To better appreciate this rotational feature, a magnified view is provided in Fig. 5 and a series of cross sections are provided in Fig. S9 within the Supplemental Material [36].

D. Irreversibility in the initial linear phase and strain localization near failure

The von Mises equivalent strain, ε_{eq}, was calculated from the displacement field, $\mathbf{u}(\mathbf{r}, t)$, obtained from DVC (Supplemental Material, Text S1 [36]). The von Mises strain indicates the presence of deviatoric strain. The time series provided in Fig. 6 clearly demonstrates nonpersistent strain localizations appearing at disparate positions across the sample, but these have not been previously reported from experimental observations over numerous time steps, as seen here. We observe the progressive development of incremental strain localization within the specimen and localization of the strain before the formation of the macroscopic specimen-spanning fault.

The primary shear band that localized along the fracture plane was consistent with reported observations of shear banding and localization in clays and other granular materials [30,45,46]. Besides this primary shear band, we also observed local shear strain that was concentrated along less-pronounced secondary shear bands. These secondary shear bands are temporary nonpersistent modes of localization, that is, localized high-strain regions, which form and eventually disappear, as observed in the specimen during the early loading stage of the test.

The first images in the top row of Fig. 6 show the influence of intermittent deformation events on the von Mises incremental strain field. This behavior is consistent with stress-induced stabilization of the specimen and the closing of preexisting fractures, as previously mentioned. The evolved structure of the von Mises strain distribution after point xiv qualitatively matches the major fracture directly observed in the tomograms, cf. Fig. 3. Figure 6(b) highlights the presence of secondary fractures in the sample. The presence of von Mises strain [Fig. 6(b)] surrounding the major fracture can be attributed to the slipping of the top section of the sample over the bottom section after fracturing.

The incremental volumetric strain field, $\varepsilon_V = \Delta V/V$, was calculated from the incremental strain tensor as described in the Supplemental Material (Text S1 [36]). This field reveals the magnitude of local dilatancy (positive values; $\Delta V/V > 0$) and compaction (negative values) in the sample. The evolving distribution of the incremental strain quantified by DVC revealed that high magnitudes of compaction, dilation, and von Mises strain were localized along the fracture (Figs. 6 and 7). In Fig. 7, a series of selected states of the time evolution of the ε_V field in the sample are shown. We observed the presence of intermittent compaction events throughout the sample that eventually localized to form the major fracture and a similar localization pattern was seen for the local dilation. These intermittent density changes are understood to be caused by the presence of weak zones in the sample and are also likely to be related to the closing of preexisting fractures or voids, as exemplified in Fig. 3. DVC analysis also identified secondary fractures that were difficult to discern directly in the tomograms, see, e.g., xv(36,36) in Fig. 7. These secondary fractures were observed to stabilize and eventually localize along the major fracture. The significant strain seen near the upper and lower ends of the sample was caused by direct contact with the pistons. Analysis of the strain evolution in the shale demonstrates that the deformations were occurring in the sample throughout the apparently linear-elastic loading stage, while strain localization was only observed in the last few time steps before macroscopic failure. Judging from Fig. 7, strain localization took place around time steps x–xii, i.e., slightly preceding or coinciding with the peak stress.

The spatially averaged volumetric strain and von Mises strain are plotted as a function of time in Fig. 8, thus providing a link between the microscopic and macroscopic behavior of the sample. Point 1 represents the minimum value for the mean volumetric strain, defined as the dilation-initiation point, with a stress, σ_{zz}, of 18 MPa, about 40% of the failure stress. This point indicates compaction of the sample, as the volumetric strain is negative, which we interpret as the closing of preexisting microcracks and collapse of pores throughout the specimen. This interpretation is supported by the results of Fig. 3 where closing of the preexisting natural fractures can be directly observed in the CT images. After point 1, the mean volumetric strain increased rapidly. In the time between points 1 and 2, small deformations dominated by rather localized dilational strains, as observed with the DVC analysis, took place. These deformations could be due to natural heterogeneity, whereas sample shifts are excluded, as they would have been readily observed in the experimental data. The fact that the loading curve resumes its steep upward trend, and that no substantial localization happens until after xi(47,46), emphasize that these are small-strain ($\ll 0.01$) events. We interpret these localized strain dilations as small inelastic (destructive) events. While time constraints during the experiment barred the performance of unload-reload cycles, such testing has been done on other samples of the same shale material (cf. Fig. S10
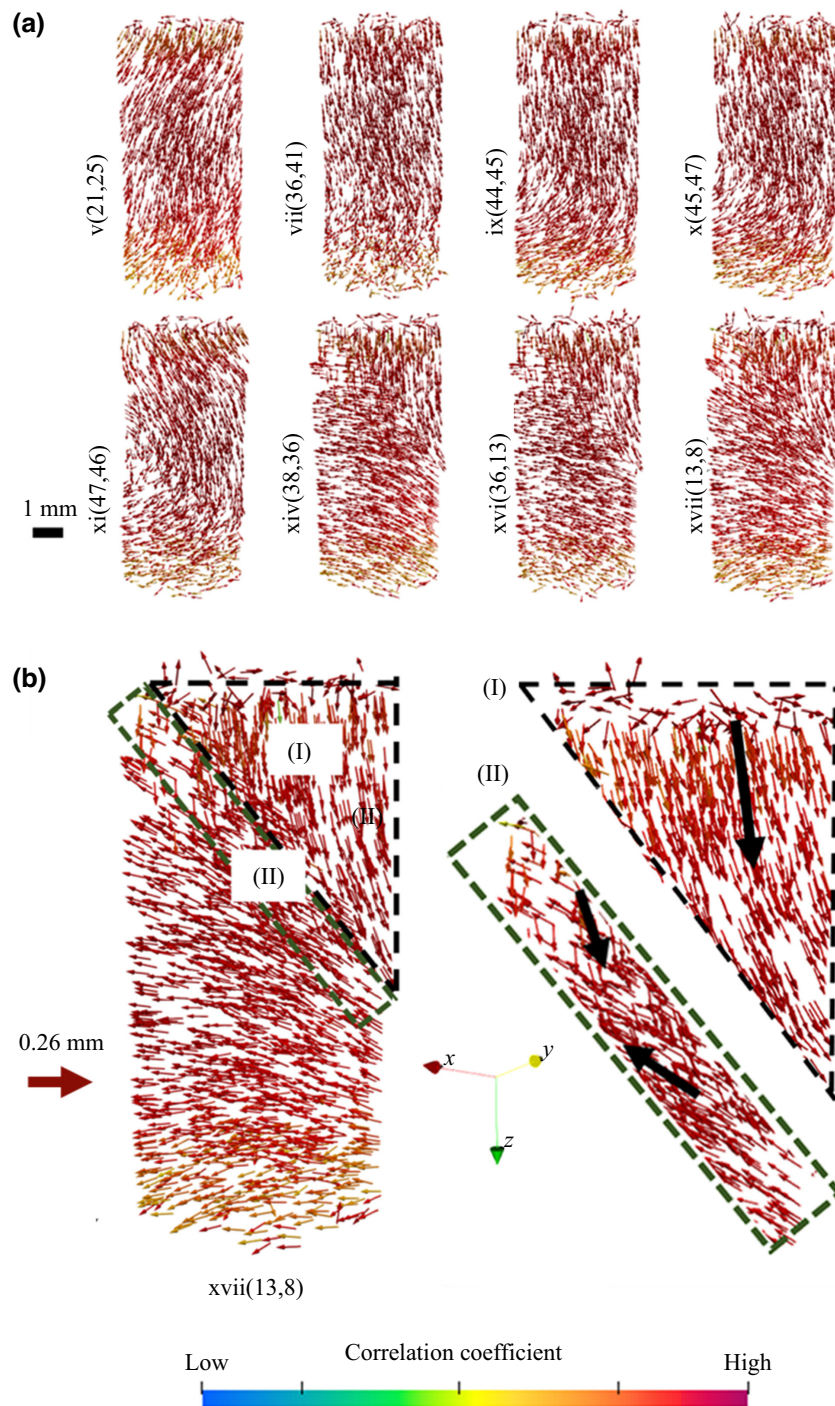
FIG. 4. Incremental displacement vector field, $\mathbf{u}(\mathbf{r}, t)$. (a) Cross-section view of $\mathbf{u}(\mathbf{r}, t)$ for selected time steps. (b) Enlarged view of xvii(13,8). Bold black arrows are guides to the eye that represent the overall movement in the sample. Color coding represents the correlation coefficient of the DVC analysis, with the prevailing red representing high correlation, indicating a reliable analysis.

within the Supplemental Material [36]), showing stress-strain behavior consistent with inelastic deformation. Note also that, while inelastic deformations would generally be expected to weaken the sample, in the compression test reported here, such weakening might be hard to detect; in other words, the stress-strain curve might still stay close to linear, as observed, after minor local compaction events. For stage B, we observe that the partitioning of strain between dilation and compaction remains almost constant with time.
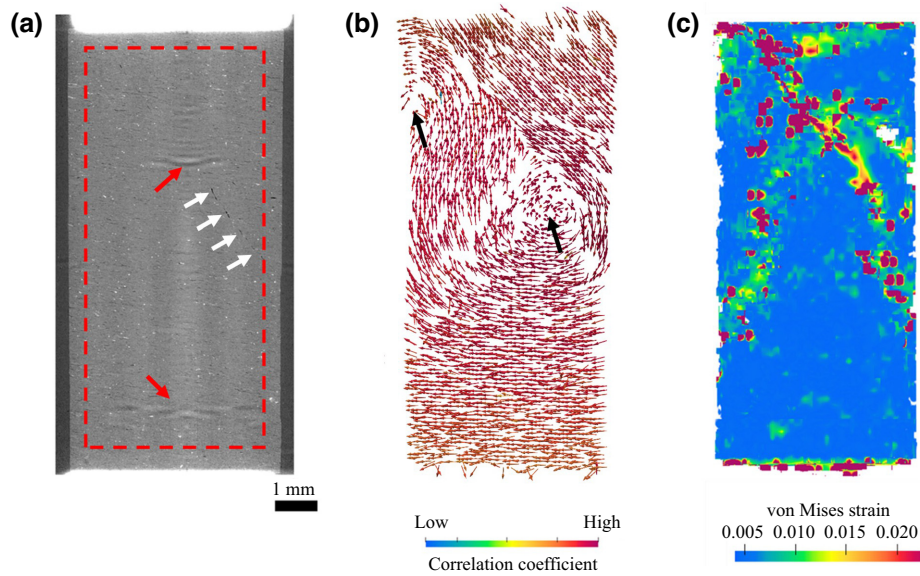
FIG. 5. Axial cross sections showing the state of the sample immediately prior to failure, at $\sigma_{zz} = 39$ MPa. (a) CT raw-data cross section. Some ring artefacts from the CT reconstruction can be seen (red arrows), and the nascent fracture is indicated by white arrows. Rectangle indicates the region of interest used for the DVC analysis. (b) Displacement field obtained from DVC interval xiii(39,38). Note the rotational nature of the displacement field, as highlighted by the two black arrows pointing to two centers of rotation on the footwall side of the inclined fault. (c) Corresponding von Mises equivalent strain. Viewing angle is specifically chosen to highlight the circular strain state in (b).

Fracture coalescence likely produces the increasing dilation observed at point 2. This point occurred at a differential stress, σ_{zz}, of 28 MPa, which was about 61% of the failure stress. Once the volumetric strain crossed zero to positive values, the volumetric strain continued to rise, perhaps due to the release and redistribution of the strain energy. It is reasonable to assert that, at this stage, the microcracks grow rapidly and eventually coalesce into a larger fracture. We observe two time steps with averaged millistrain values of >0.5, as indicated by points 3 and 4 in Fig. 8, following major drops in the axial stress.

IV. DISCUSSION

Motivated by the prospect of CO_2 and H_2 storage in abandoned oil and gas reservoirs in the North Sea, the experiment reported here contains several results that are of particular interest. Until recently, CO_2 has mainly been stored in saline aquifers, which are large layers of permeable sandstone filled with brine. The resident brine is displaced by CO_2 during injection. The extent of these reservoirs helps maintain the final fluid pore pressure at a level not too high compared to what it was before injection. To maximize the injected mass, CO_2 is preferably kept in its supercritical phase. Consequently, for the temperature expected after compression and given some heating at the well head, the reservoirs considered should be deeper than 700 m. For depleted (abandoned) oil and gas reservoirs, the depth is typically more than 2 km below the seafloor, which roughly corresponds to a pore pressure of >20 MPa and vertical stress of >40 MPa for the reservoir, considering an average material density of >2000 kg/m^3. H_2 storage will be in gaseous form and will rely mostly on abandoned fields, with smaller volumes needed compared to CO_2. Consequently, there is no particular depth requirement, except that several caprock and overburden barriers should be present to prevent leakage. Since most North Sea production fields are 2–5 km below the seabed, H_2 will be stored at these depths with the same pressure and stress values as noted above.

Since we are discussing the overlying shale caprock in this article, the stress values could be slightly lower (the Draupne core was obtained from around 1970 m depth). Additionally, for the experiments reported here, we had to consider the admissible pressure ranges of the HADES cell and the precision in maintaining the pressure at different levels. Relevance for natural climate solutions was our primary concern in these tests, and we tried to mimic pressure conditions, while, at the same time, working within the time limits of the allotted time slot at the synchrotron, which dictated the maximum permissible peak stress and the minimum strain rate for reaching peak stress. These constraints enforced some compromises, as ideally one would prefer the pore pressure not to increase too quickly during the stress changes for these low-permeability rocks.
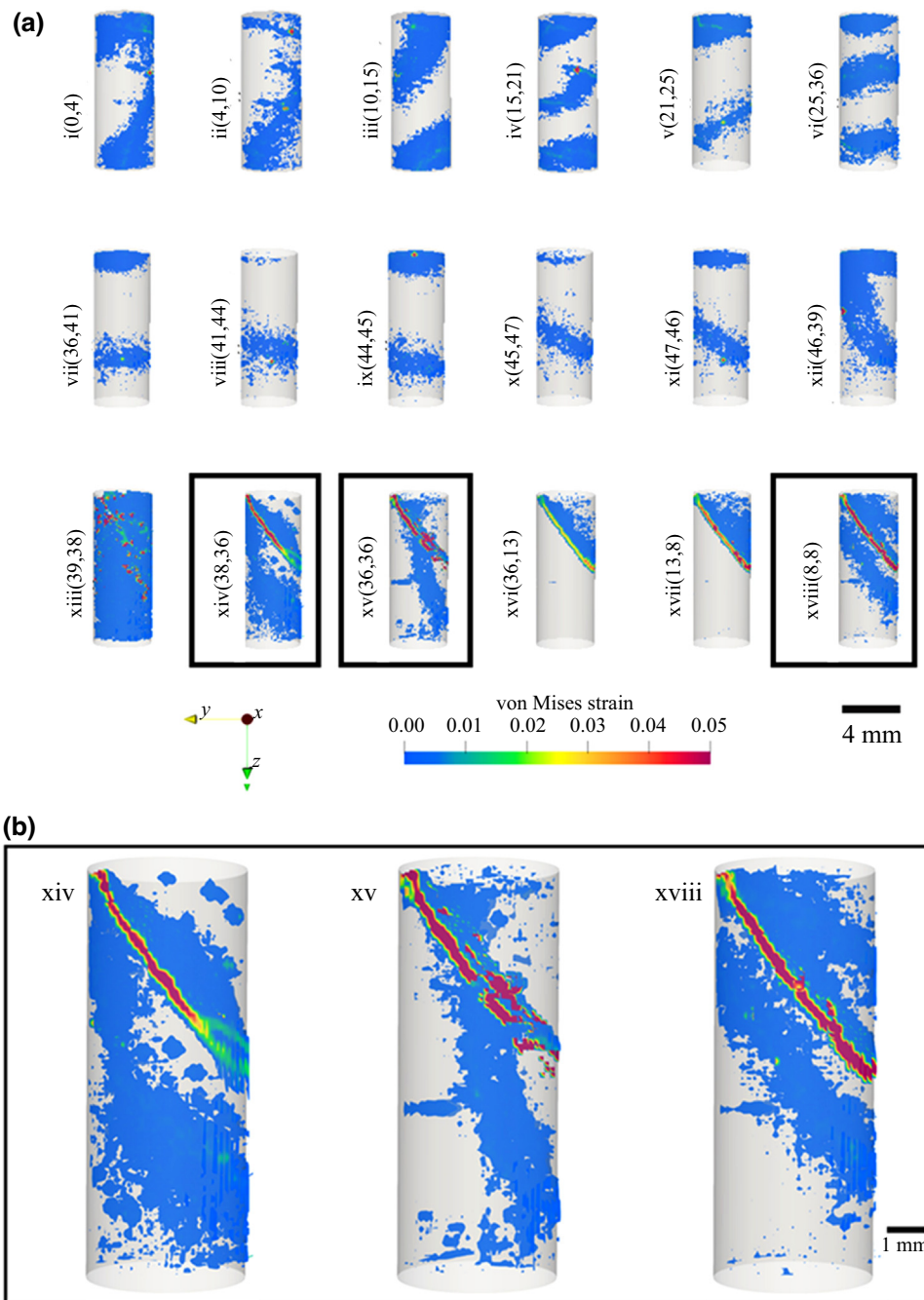
FIG. 6.   Perspective view of the von Mises equivalent incremental strain, ε_{eq}, for stage A. (a) In about the first 10 time steps, strain distribution varies apparently randomly from one time step to the next. Strain appears to localize at about time step x, and the sample ruptures near xiii. (b) Enlarged views of strain states xiv, xv, and xviii. Primary shear band has $\varepsilon_{eq} > 0.05$ (red in the figure), and secondary features with significantly lower strain (blue) are also seen. Note that ε_{eq} values of zero are rendered as transparent.

From knowledge of the permeability, the pressure diffusion time can be estimated, assuming an incompressible pore fluid [47]. In designing such triaxial tests, one can adopt two paths: either (i) use the net stress principle, i.e., that failure occurs in the rock when the stress-pore pressure exceeds the strength limit, and thus, one can lower the applied pore pressure relative to the *in situ* value; or (ii) try to operate as close to *in situ* conditions as possible. We chose the second approach, moderated by the above constraints.

A conceivably critical observation in our study is that the apparently linear stress-strain curve in fact contains
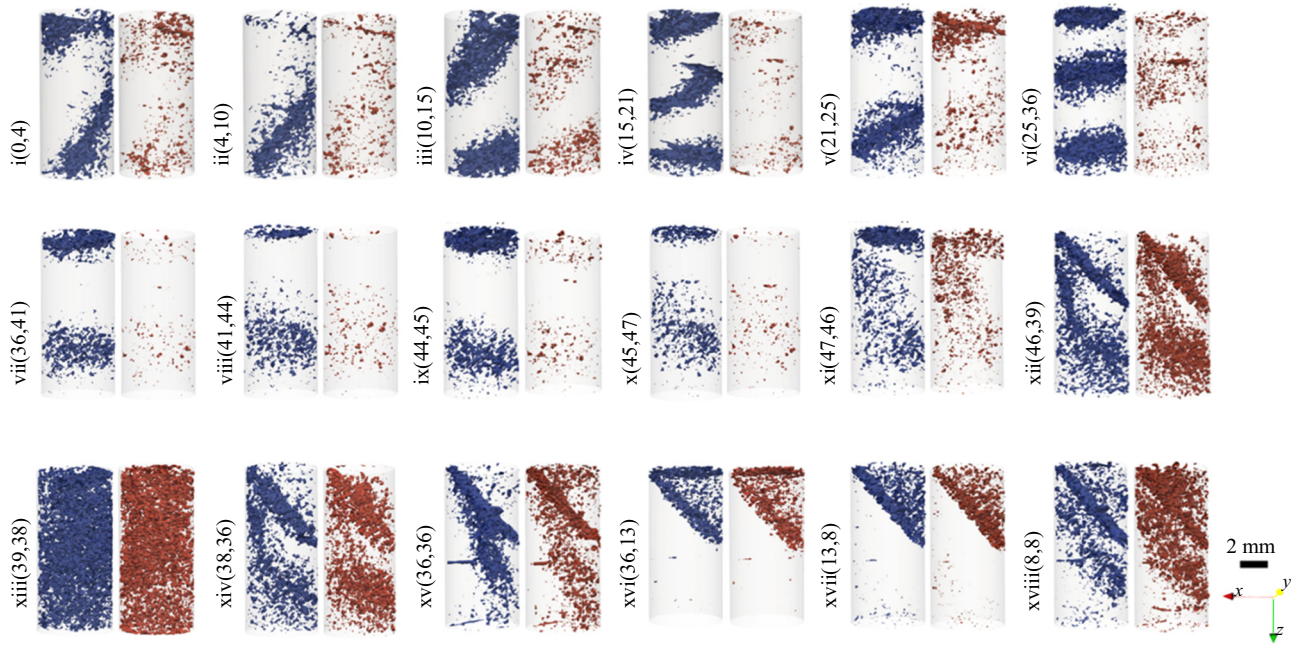
FIG. 7. Perspective visualizations of the volumetric strain evolution in stage A. Images are split into pairs to show the spatial distribution of compaction, $\varepsilon_V < 0$ (left, blue), and dilation, $\varepsilon_V > 0$ (right, red). Blue isosurfaces represent incremental compaction ε_V in the range $(-0.6, -0.005)$, and red isosurfaces are dilative incremental ε_V in the range $(0.005, 0.6)$, with ranges chosen to highlight the dynamics. Gray shaded cylinder outline is an idealized (truncated) representation of the region of interest used for the DVC analysis.

a series of intermittent minor strain events taking place at random locations within the specimen. As elaborated below, we have reason to believe that these strain events are irreversible and destructive. Arguably, the Young's modulus could thus be somewhat higher than that prescribed by the straight line in Fig. 2, perhaps by a factor of 2–5, as suggested by the smaller irregularities of the curve. It is widely known that shales are highly brittle, and the yielding point indicated in Fig. 2 could be an unrealistically high stress value. Specifically, the value of (39 ± 2) MPa should not be interpreted as the maximum stress the Draupne shale sample can endure elastically. Furthermore, the apparently random locations of the intermittent events observed in the strain evolution indicated that the specimen was highly uniform; otherwise, one might expect the strain localization and subsequent failure to be confined to the weakest region of the sample.

Supported by the experiments, we argue that, despite the linear stress-strain curve up to semibrittle failure, irreversible damage occurs in the rock, and we cannot qualify this behavior under initial loading as being linear elastic. This quite intriguing observation can be addressed if we compare the strains incurred in the sporadic events shifting location to expectations given the known smallest elastic moduli of the mineral constituents of grains and grain cement, as well as clay stacks, as a function of stress increments over the time lapse for DVC. We

have also seen this linear behavior in other shales, where, invariably, if unload-reload loops are incorporated into the triaxial test, the unload slope is steeper than the master load slope (see also Fig. S10 within the Supplemental Material [36]). We note, of course, that this response is very different from that of a typical metal-bar elongation test, which exhibits a plastic yield point, then work hardening or softening until peak stress-associated failure. The observed behavior is indicative of two related phenomena: (1) the presence of a mixture of recoverable (elastic) and irreversible (plastic, damage) deformation upon loading, where unloading reveals plastic deformation; and (2) the master loading curve is characterized by "fresh" grain-bond destruction events that are self-similar in the sense that new small regions of intact rock get damaged as the axial stress is increased, and therefore, the same straight slope is observed.

The highly rotational strain state observed in 3D immediately prior to failure was not previously reported in microscopic rock studies but has been well described intuitively and theoretically [44]. Our study gives detailed and important insights into the failure of a comparably minute piece of shale from the Draupne formation, triggering the questions of representativity and upscaling. This consequence of limited synchrotron access is likely to be reduced in the future, as experiments that are feasible in university laboratories keep evolving at a rapid pace.
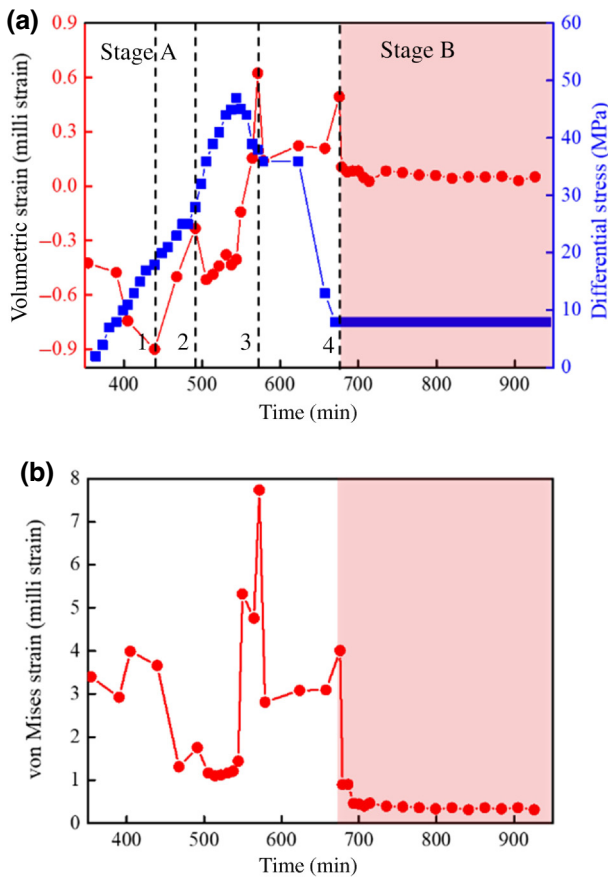
FIG. 8. Strain evolution spatially averaged over the entire sample. (a) Volumetric strain (red circles) and axial stress (blue squares) plotted as a function of elapsed time. Point 1 marks the initiation of dilation, point 2 is the initiation of microcracks, and points 3 and 4 indicate large incremental volumetric-strain-drop events. (b) von Mises equivalent strain.

V. CONCLUSION

Here, we studied how a shale caprock sample was brought to failure under reservoir conditions. Specifically, a Draupne shale sample was investigated through triaxial testing monitored by synchrotron-based microcomputed tomography and digital volume-correlation analysis. We described quantitatively the sample evolution towards failure. Most importantly, we provided data indicating that the initial linear stress-strain phase contained irreversible deformations. The onset of failure occurred by an increase of dilation and a pronounced high-shear state, as previously reported for Green River shale [31]. Tracking the evolution of the 3D incremental displacement field in the sample (Fig. 4), we observed early nonhomogenous deformations, including intermittent strain clustering at apparently random locations. After fracture, a sliding-block mechanism was observed. By following the evolution of the volumetric and von Mises strains, the temporary localization that occurred in the sample prior to the formation of

the macroscopic fault was revealed. The creep observed on this macroscopic fault indicated that the slow deformations in the shale could be related to the slip on the surface and not only to bulk creep. This study also revealed the presence of the secondary fracture networks that connected to the system-spanning fault in the sample at different stages of the experiment; these features are important to understand the failure of shales and have not previously been reported. The experimental and analysis techniques presented herein reveal the local mechanics in the Draupne shales and can further be applied to understand the stability of these rocks for applications like CO_2 sequestration.

[1] M. F. Ashby and S. D. Hallam, The failure of brittle solids containing small cracks under compressive stress states, Acta Metall. **34**, 497 (1986).

[2] J. F. W. Gale, S. E. Laubach, J. E. Olson, P. Eichhubl, and A. Fall, Natural fractures in shale: A review and new observations, AAPG Bull. **98**, 2165 (2014).

[3] B. L. Alemu, P. Aagaard, I. A. Munz, and E. Skurtveit, Caprock interaction with CO_2: A laboratory study of reactivity of shale with supercritical CO_2 and brine, Appl. Geochem. **26**, 1975 (2011).

[4] N. Agofack, P. Cerasi, E. Sonstebo, and J. Stenebraten, Thermo-poromechanical properties of Pierre II shale, Rock Mech. Rock Eng. **55**, 6703 (2022).

[5] E. Skurtveit, E. Aker, M. Soldal, M. Angeli, and Z. Wang, Experimental investigation of CO_2 breakthrough and flow mechanisms in shale, Pet. Geosci. **18**, 3 (2012).

[6] Z. H. Zhang and D. Huisingh, Carbon dioxide storage schemes: Technology, assessment and deployment, J. Cleaner Prod. **142**, 1055 (2017).

[7] G. P. D. De Silva, P. G. Ranjith, and M. S. A. Perera, Geochemical aspects of CO_2 sequestration in deep saline aquifers: A review, Fuel **155**, 128 (2015).

[8] C. M. White, B. R. Strazisar, E. J. Granite, J. S. Hoffman, and H. W. Pennline, Separation and capture of CO_2 from large stationary sources and sequestration in geological formations - coalbeds and deep saline aquifers, J. Air Waste Manage. Assoc. **53**, 645 (2003).

[9] B. Jia, Z. Chen, and C. Xian, Investigations of CO_2 storage capacity and flow behavior in shale formation, J. Pet. Sci. Eng. **208,** 109659 (2022).

[10] M. Bui, C. S. Adjiman, A. Bardow, E. J. Anthony, A. Boston, S. Brown, P. S. Fennell, S. Fuss, A. Galindo, L. A. Hackett, et al., Carbon capture and storage (CCS): The way forward, Energy Environ. Sci. **11,** 1062 (2018).

[11] E. K. Halland, F. Riis, C. Magnus, W. T. Johansen, I. M. Tappel, I. T. Gjeldvik, T. Solbakk, and V. T. H. Pham, CO_2 storage atlas of the Norwegian part of the North Sea, Energy Procedia **37,** 4919 (2013).

[12] M. Josh, L. Esteban, C. Delle Piane, J. Sarout, D. N. Dewhurst, and M. B. Clennell, Laboratory characterisation of shale properties, J. Pet. Sci. Eng. **88-89,** 107 (2012).

[13] S. Kelly, H. El-Sobky, C. Torres-Verdin, and M. T. Balhoff, Assessing the utility of FIB-SEM images for shale digital rock physics, Adv. Water Resour. **95,** 302 (2016).

[14] V. Cnudde and M. N. Boone, High-resolution x-ray computed tomography in geosciences: A review of the current technology and applications, Earth-Sci. Rev. **123,** 1 (2013).

[15] F. Renard, J. McBeck, B. Cordonnier, X. J. Zheng, N. Kandula, J. R. Sanchez, M. Kobchenko, C. Noiriel, W. L. Zhu, P. Meakin, et al., Dynamic in situ three-dimensional imaging and digital volume correlation analysis to quantify strain localization and fracture coalescence in sandstone, Pure Appl. Geophys. **176,** 1083 (2019).

[16] M. J. Blunt, B. Bijeljic, H. Dong, O. Gharbi, S. Iglauer, P. Mostaghimi, A. Paluszny, and C. Pentland, Pore-scale imaging and modelling, Adv. Water Resour. **51,** 197 (2013).

[17] F. Renard, J. McBeck, N. Kandula, B. Cordonnier, P. Meakin, and Y. Ben-Zion, Volumetric and shear processes in crystalline rock approaching faulting, Proc. Natl. Acad. Sci. U. S. A. **116,** 16234 (2019).

[18] E. A. Chavez Panduro, B. Cordonnier, K. Gawel, I. Børve, J. Iyer, S. A. Carroll, L. Michels, M. Rogowska, J. A. McBeck, H. O. Sørensen, et al., Real time 3D observations of Portland cement carbonation at CO_2 storage conditions, Environ. Sci. Technol. **54,** 8323 (2020).

[19] Y. Geraud, F. Mazerolle, S. Raynaud, and P. Lebon, Crack location in granitic samples submitted to heating, low confining pressure and axial loading, Geophys. J. Int. **133,** 553 (1998).

[20] F. Renard, B. Cordonnier, D. K. Dysthe, E. Boller, P. Tafforeau, and A. Rack, A deformation rig for synchrotron microtomography studies of geomaterials under conditions down to 10 km depth in the Earth, J. Synchrotron Radiat. **23,** 1030 (2016).

[21] S. Raynaud, G. Vasseur, B. Celerier, D. Loggia, M. Ghoreychi, M. H. Mathon, and F. Mazerolle, Experimental study of the relation between the permeability of kaolinite and its deformation at micro and macro scale, Int. J. Rock Mech. Min. Sci. **47,** 559 (2010).

[22] E. M. Charalampidou, S. A. Hall, S. Stanchits, H. Lewis, and G. Viggiani, Characterization of shear and compaction bands in a porous sandstone deformed under triaxial compression, Tectonophysics **503,** 8 (2011).

[23] E. Tudisco, M. Etxegarai, S. A. Hall, E. M. Charalampidou, G. D. Couples, H. Lewis, A. Tengattini, and N. Kardjilov, Fast 4-D imaging of fluid flow in rock by high-speed neutron tomography, J. Geophys. Res.-Solid Earth **124,** 3557 (2019).

[24] E. Tudisco, S. A. Hall, E. M. Charalampidou, N. Kardjilov, A. Hilger, and H. Sone, in *10th World Conference on Neutron Radiography (WCNR)* (Elsevier Science Bv, Grindelwald, Switzerland, 2014), pp. 509.

[25] F. K. Murer, A. S. Madathiparambil, K. R. Tekseth, M. Di Michiel, P. Cerasi, B. Chattopadhyay, and D. W. Breiby, Orientational mapping of minerals in Pierre shale using x-ray diffraction tensor tomography, IUCrJ **8,** 747 (2021).

[26] W. De Boever, A. Diaz, H. Derluyn, T. De Kock, J. Van Stappen, J. Dewanckele, T. Bultreys, M. Boone, T. De Schryver, E. T. B. Skjonsfjell, et al., Characterization of composition and structure of clay minerals in sandstone with ptychographic x-ray nanotomography, Appl. Clay Sci. **118,** 258 (2015).

[27] B. Chattopadhyay, A. S. Madathiparambil, F. K. Murer, P. Cerasi, Y. Chushkin, F. Zontone, A. Gibaud, and D. W. Breiby, Nanoscale imaging of shale fragments with coherent x-ray diffraction, J. Appl. Crystallogr. **53,** 1562 (2020).

[28] B. K. Bay, T. S. Smith, D. P. Fyhrie, and M. Saad, Digital volume correlation: Three-dimensional strain mapping using x-ray tomography, Exp. Mech. **39,** 217 (1999).

[29] E. Tudisco, E. Ando, R. Cailletaud, and S. A. Hall, TomoWarp2: A local digital volume correlation code, SoftwareX **6,** 267 (2017).

[30] E. Fjær, R. M. Holt, P. Horsrud, and A. M. Raaen, *Petroleum related rock mechanics*, 2nd ed. (Elsevier, Amsterdam, 2008).

[31] J. McBeck, M. Kobchenko, S. A. Hall, E. Tudisco, B. Cordonnier, P. Meakin, and F. Renard, Investigating the onset of strain localization within anisotropic shale using digital volume correlation of time-resolved x-ray microtomography images, J. Geophys. Res.-Solid Earth **123,** 7509 (2018).

[32] J. Rahman, M. Fawad, and N. H. Mondol, Organic-rich shale caprock properties of potential CO_2 storage sites in the northern North Sea, offshore Norway, Mar. Pet. Geol. **122,** 104665 (2020).

[33] J. A. Hansen, N. H. Mondol, and M. Fawad, Organic content and maturation effects on elastic properties of source rock shales in the central North Sea, Interpretation **7,** T477 (2019).

[34] D. Paganin, S. C. Mayo, T. E. Gureyev, P. R. Miller, and S. W. Wilkins, Simultaneous phase and amplitude extraction from a single defocused image of a homogeneous object, J. Microsc. **206,** 33 (2002).

[35] A. Mirone, E. Brun, E. Gouillart, P. Tafforeau, and J. Kieffer, The PyHST2 hybrid distributed code for high speed tomographic reconstruction with iterative reconstruction and a priori knowledge capabilities, Nucl. Instrum. Methods Phys. Res., Sect. B **324,** 41 (2014).

[36] See the Supplemental Material at http://link.aps.org/supplemental/10.1103/PhysRevApplied.20.034046 for details on the strain calculation, principal component analysis, effect of node spacing, and Skempton A coefficient.

[37] N. Agofack, P. Cerasi, A. Stroisz, and S. Rørheim, in *53rd U.S. Rock Mechanics/Geomechanics Symposium* (2019).

[38] M. J. Turunen, S. Le Cann, E. Tudisco, G. Lovric, A. Patera, S. A. Hall, and H. Isaksson, Sub-trabecular strain

evolution in human trabecular bone, Sci. Rep. **10,** 13788 (2020).

[39] S. Heng, X. Z. Li, X. Liu, and Y. Chen, Experimental study on the mechanical properties of bedding planes in shale, J. Nat. Gas Sci. Eng. **76,** 103161 (2020).

[40] M. Soldal, E. Skurtveit, and J. C. Choi, Laboratory evaluation of mechanical properties of Draupne shale relevant for CO_2 seal integrity, Geosciences **11,** 244 (2021).

[41] F. Renard, B. Cordonnier, M. Kobchenko, N. Kandula, J. Weiss, and W. L. Zhu, Microscale characterization of rupture nucleation unravels precursors to faulting in rocks, Earth Planet. Sci. Lett. **476,** 69 (2017).

[42] W. F. Chen and D. J. Han, *Plasticity for Structural Engineers* (Springer, New York, 2011).

[43] P. Bésuelle, J. Desrues, and S. Raynaud, Experimental characterisation of the localisation phenomenon inside a Vosges sandstone in a triaxial cell, Int. J. Rock Mech. Min. Sci. **37,** 1223 (2000).

[44] D. D. Pollard and P. Segall, in *Fracture Mechanics of Rock*, edited by B.K. Atkinson (Academic Press, London, 1987), p. 277.

[45] A. Aydin, R. I. Borja, and P. Eichhubl, Geological and mathematical framework for failure modes in granular rock, J. Struct. Geol. **28,** 83 (2006).

[46] J. Desrues and G. Viggiani, Strain localization in sand: An overview of the experimental results obtained in Grenoble using stereophotogrammetry, Int. J. Numer. Anal. Methods Geomech. **28,** 279 (2004).

[47] P. Cerasi, E. Lund, M. L. Kleiven, A. Stroisz, S. Pradhan, C. Kjøller, P. Frykman, and E. Fjær, Shale creep as leakage healing mechanism in CO_2 sequestration, Energy Procedia **114,** 3096 (2017).